Hindawi
Advances in Civil Engineering
Volume 2021, Article ID 6677992, 14 pages
https://doi.org/10.1155/2021/6677992

Research Article

Experimental Study on the Difference of Shale Mechanical Properties

Qi Liu, Bing Liang, Weiji Sun, and Hang Zhao

School of Mechanics and Engineering, Liaoning Technical University, Fuxin 123000, China

Correspondence should be addressed to Qi Liu; 471910003@stu.lntu.edu.cn

Received 7 December 2020; Revised 27 April 2021; Accepted 21 May 2021; Published 4 June 2021

Academic Editor: Elhem Ghorbel

This paper studies the anisotropic characteristics of shale and the difference in mechanical performance between deep shale and outcrop shale. The outcrop shale was collected from the Shuanghe section in Changning County, southern Sichuan, and the deep shale was collected from the Wells Yi201 and Lu202. Study their basic mechanical parameters, failure modes, and wave velocity responses through laboratory tests. Research shows that with the increase of bedding angle, the deformation mode has the trend from elastic deformation to plastic deformation in high-stress state. When the bedding angles are 0°, 30°, and 45°, the weak bedding surface plays a leading role in the formation of the failure surface trend. As the bedding angle increases to 60° and 90°, its influence is weakened. The tensile strength, elastic modulus, and wave velocity decrease with the increase of bedding angle. The compressive strength and Poisson's ratio have the law of U-type change, there are higher values at 0° and 90°, and the lowest values are at 30°. The brittleness index first increases and then decreases with the increase of the bedding angle. The tensile strength and Poisson's ratio of outcrop shale and deep shale are close, but the compressive strength of deep shale is only 1/3 of outcrop shale, the elastic modulus is only 3/4 of outcrop shale, and the failure of deep shale is accompanied by instability failure.

1. Introduction

Shale gas will play an important role in the global energy structure in the future [1, 2]. Shale is not only the source rock but also the reservoir of shale gas. Its mechanical characteristics in different directions (that is anisotropy) are one of the important factors to be considered in shale gas drilling stability, hydraulic fracturing design, and field construction [3–6].

At present, many scholars have made great progress in the study of shale anisotropy. Jaeger et al. [7] has carried on the pioneering research to the anisotropic destruction criterion of rock materials. Lekhnitskii et al. [8] general equation of anisotropic elastic theory is derived, which provides a theoretical basis for the study of anisotropic problems. On these bases, Nova [9] and Cazacu et al. [10] and Lee and Pietruszczak [11] put forward different anisotropic strength criteria. Vernik and Nur [12] studied the wave velocity anisotropy of black organic shale and concluded that the anisotropy of black shale is mainly caused by its own microstructure. Niandou et al. [13] have carried out triaxial tests and addition and unloading tests on shale. The test results show that shale has obvious anisotropic characteristics and has two failure modes: shear failure and tension failure. Cho et al. [14] studied the anisotropy of elastic parameters and strength of gneiss, shale, and schist at different angles through uniaxial compression and Brazilian splitting tests. Sone and Mark [15], through the comparison of shale anisotropy in different blocks, considered that shale anisotropy increases with the increase of clay and organic matter content. Chalmers et al. [16] investigated the nanopore system of gas shale by using scanning electron microscope and got the rule that the pores parallel to the bedding direction are larger. Li et al. [17] defined the stress threshold to study the crack evolution process and gave the conclusion that crack damage stress, crack initiation strain, and crack damage strain are strongly dependent on the bedding layer inclined angle. Wang et al. [18] concluded that the maximum shear strength of shale is 60° based on the experimental data. Through the Brazilian split test and three-point bending test, Jin et al. [19] discussed the anisotropy of shale fracture behavior. Tang and Wu [20] gave the

anisotropic crack evolution characteristics of shale and mudstone in laboratory experiments. Ma et al. [21] proposed a novel theoretical method to underpin the failure mechanisms of anisotropic rocks under Brazilian test conditions. Gui et al. [22, 23] reported on anisotropic damage of shale stress coupled with hydration and proposed the conclusion that damage parameters parallel to bedding are greater than those perpendicular to bedding. Wan et al. [24] analyzed the anisotropy of the diffusivity of gas shale, and the diffusivity is much higher at the parallel to the bedding direction than that at perpendicular direction.

The shale has obvious bedding characteristics under the influence of deposition mode. The existing studies show that the shale mechanical parameters of different blocks are diversified, coupled with the heterogeneity of shale and the difficulty of sample preparation far, and there is no conclusion on the complete system of shale anisotropy. Based on the previous research experience, this paper makes an in-depth study of outcrop shale of Longmaxi Formation in Sichuan Basin on the difference of multidirectional mechanical properties of shale. The stress-strain curve, compressive strength, tensile strength, elastic modulus, Poisson's ratio, brittleness index, and failure mode of shale during shale failure are analyzed. The anisotropy of mechanical parameters is compared, and the elastic constants of Longmaxi shale based on transverse isotropic model are obtained.

In addition, the basic research of shale mechanical parameters is used for underground shale gas exploration. Most of the existing research data are the results of outcrop shale measurements. The mechanical properties of outcrop/deep shale are not completely the same due to the influence of stratum structure, light, and temperature and cannot be applied arbitrarily. Therefore, this paper selects the deep shale of Longmaxi Formation in Sichuan Basin, China, to carry out general mechanical experiments, and makes a comparative analysis and summary of the similarities and differences between outcrop and deep shale mechanical parameters, in order to better match and apply the existing research results of outcrop shale anisotropy to deep shale gas reservoir exploitation in the future and provide basic data support for shale gas exploration and development.

2. Experimental Samples and Scheme

2.1. Experimental Sample. The southern Sichuan Basin is the largest shale gas production base in China. In recent years, PetroChina has vigorously promoted the exploration and development of shale gas resources in southern Sichuan, in which the Longmaxi Formation shale is the main exploration block [25]. Therefore, this paper selects the Longmaxi Formation shale as the research object. The outcrop shale sample is located in Shuanghe section of Changning County, Yibin City, Sichuan Province. This section is exposed to relatively complete and easy to sample around the quarry. The deep shale samples were collected from Well Yi201 in Changning shale gas exploitation block and from Well Lu202 in Luzhou block, respectively, two groups of samples are located in Long 1_1^1 strata of Longmaxi Formation (see document [26] for stratigraphic division), and the specific location is shown in Figure 1.

Large shale samples without weathering and with obvious bedding characteristics were selected from the surface. Establish a Cartesian coordinate system based on bedding plane, as shown in Figure 2(a), and prepare standard shale sample with diameter of 25 mm and height diameter ratio of 2 : 1 according to GB/T 50266-2013 standard practice [27]. According to different azimuth angle α and bedding angle β (the angle between axial loading direction and sedimentary bedding plane of sample is shown in Figures 2(c) and 2(d)), shale samples in 12 directions were prepared as shown in Figure 2(b). To ensure that the samples are located in the same coordinate system, all standard shale samples are made on the same large shale sample. A total of 72 outcrop shale samples and 6 deep shale samples are obtained in this test, as shown in Figure 3.

2.2. Experimental Equipment and Scheme. Shale uniaxial compression test and Brazilian splitting test instruments use SANS CMT-5504 electronic universal testing machine with maximum axial load up to 1000 kN and strain data recorded by the DH5923N dynamic signal test and analysis system with accuracy less than 0.5%. Displacement loading control is used in loading mode, and the rate is set 0.02 mm/s. The instrument for measuring wave velocity is based on DS5-8B series full information acoustic emission signal analyzer, whose probe frequency is 50~400 KHz and the center frequency is 150 KHz. The specific research programme is shown in Table 1.

3. Analysis on Difference of Mechanical Performance of Shale in Different Directions

3.1. Analysis of the Variation of Stress-Strain Curve with Bedding Angle. The stress-strain curves of outcrop shale with square angle $\alpha = 0^\circ$, 30°, 45°, 60°, and 90° (coring directions 1, 9, 10, 11, and 12) are shown in Figure 4. The stress-strain curves of outcrop shale of Longmaxi Formation show no obvious distinction in each stage, which indicates that shale is typical brittle rock. The initial positions of stress-strain curves of five different bedding angles are all similar to straight lines, and the difference between the initial compaction stage and the linear elastic stage is not obvious, which indicates that there is no obvious compaction stage; the elastic stage of the curve is long, and the distinction between the elastic limit and the plastic limit is not obvious, especially the curves of 0°, 30°, and 45°; after the curve reaches its peak value, the curve drops to its lowest value immediately, and it has typical brittle failure characteristics.

The stress-strain curves of 5 different bedding angles coincide at the initial compaction stage, and the strain increases gradually with the increase of axial stress. The turning point of 5 curve strike occurs near the axial strain $\varepsilon = 4.22 \times 10^{-3}$. The five curves show different trends, from top to bottom, which are 0°, 30°, 45°, 60°, and 90° bedding angle. The larger bedding angle, the lower slope, indicating that the elastic modulus decreases gradually with the increase of bedding angle.

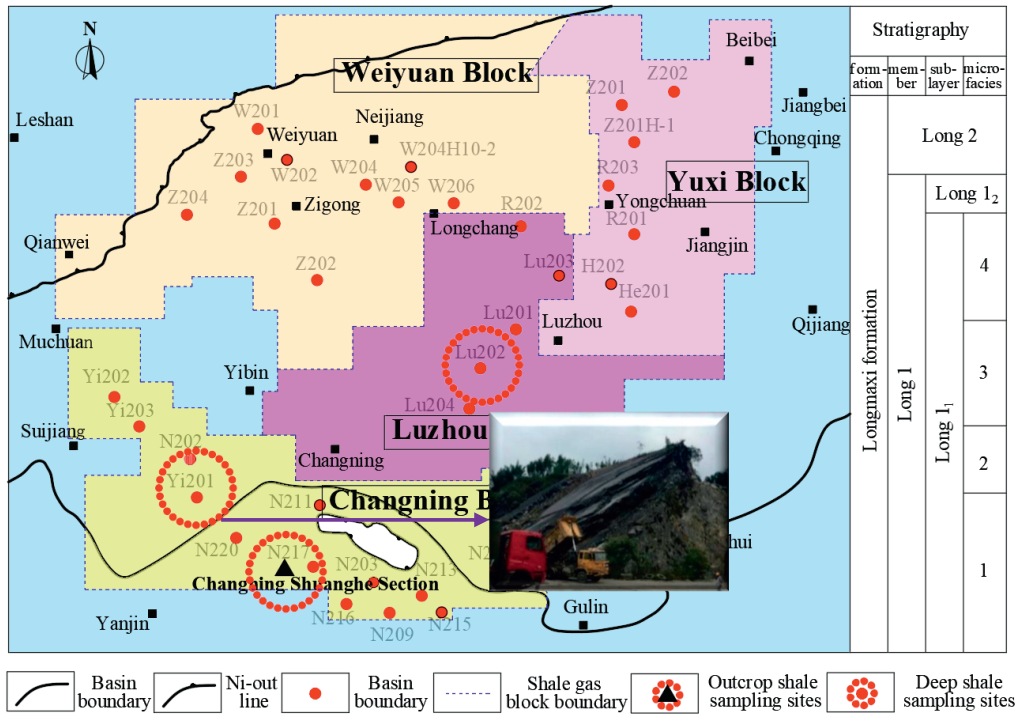

Figure 1: Sampling site and stratigraphic histogram.

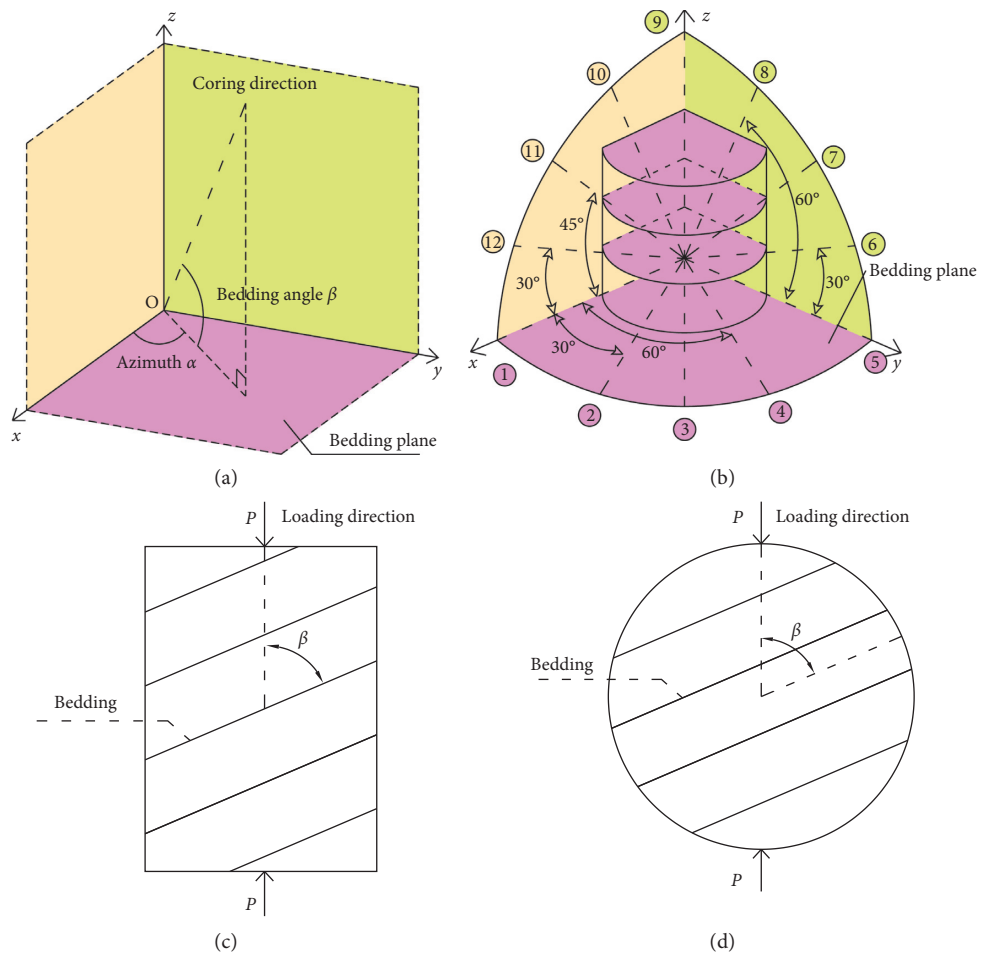

Figure 2: Schematic diagram of multidirectional sample preparation. (a) Azimuth angle and bedding angle in the coordinate system. (b) Sample drilling direction. (c) Direction of bedding angle in uniaxial compression experiment. (d) Direction of bedding angle in Brazilian splitting experiment.

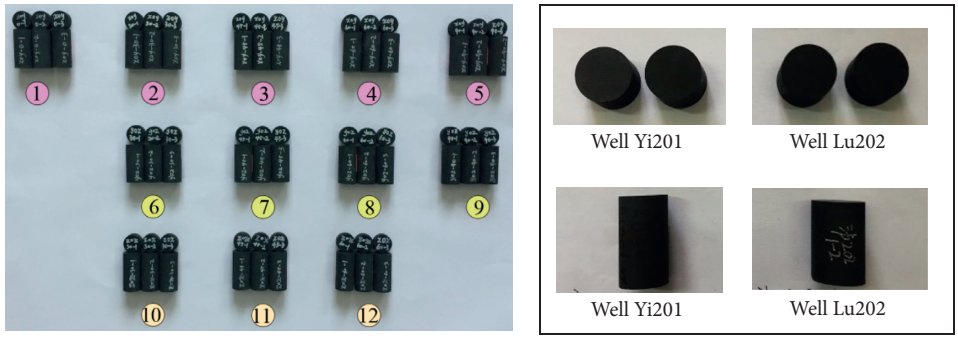

(a) (b)

Figure 3: Shale sample. (a) Multidirectional outcrop shale sample. (b) Deep shale sample.

Table 1: Research categories and objectives.

Experimental category	Shale type	Bedding angle/azimuth	Objective
Uniaxial compression	Outcrop shale	0°, 30°, 45°	Anisotropy
Brazilian splitting		60° and 90°	Transversely isotropic
Wave velocity	Deep shale	90°	Deep/outcrop shale comparison of mechanical performance

The change of bedding angle will affect the deformation mode before the sample is destroyed. The elastic stage of the stress-strain curve is longer, especially the curve of 0°, 30°, and 45° approaches a straight line, indicating that most of the deformation is elastic after compaction and before the failure of the specimens. When the bedding angle increases to 60° and 90°, the slope of the curve decreases in the high-stress section before the sample is destroyed, which indicates that the curve has plastic deformation after reaching the elastic limit. With the increase of bedding angle, the loading deformation of shale under high stress tends to change from elastic deformation to plastic deformation. The larger the bedding angle, the longer the plastic deformation stage.

3.2. Analysis of the Variation of Shale Failure Type with Bedding Angle. Because of the tight nature of shale, bedding as a weak surface is the main factor affecting the type of shale failure. The experimental results show that there are two main failure modes of shale under uniaxial load: tensile splitting failure and shear failure. The failure modes with different bedding angles are shown in Figure 5.

(1) When $\beta = 0°$, the failure type is vertical splitting tensile failure along the bedding surface. After failure, multiple tensile failure planes parallel to the bedding plane are formed through the two ends of the specimen. The specimens are separated into a plurality of vertical long strip flake rock blocks.

(2) When $\beta = 30°$, the failure type is shear failure along the bedding plane. After failure, a single shear failure surface along the weak plane of bedding is formed, accompanied with vertical microcracks. There is obvious shear slip along the bedding plane direction.

(3) When $\beta = 45°$, the failure type is a mixture of shear failure along bedding plane and Y-type shear failure. After failure, a shear failure surface along the weak plane of bedding is formed. Under the influence of the end effect, a Y-type shear failure surface is formed at the end of the specimen.

(4) When $\beta = 60°$, the failure type is a mixture of vertical splitting failure and Y-type shear failure. After fracture, inclined shear failure surface and vertical splitting failure surface are formed passing through many bedding planes. The failure is accompanied by loud noise, and the sample is easy to burst into small rock blocks.

(5) When $\beta = 90°$, the failure type is a mixture of splitting tension failure of the cross-cut bedding plane and shear failure along the direction of the bedding. After failure, the vertical splitting failure surface and the transverse failure surface along the bedding plane are formed. The two failure surfaces are intersecting.

The experimental results show that with the increase of bedding angle, the failure mode of shale firstly changes from vertical splitting tensile failure to shear slip failure along the weak bedding plane and finally evolves into splitting tension failure of the cross-cut bedding plane. When the bedding angles are 0°, 30°, and 45°, the weak bedding surface plays a leading role in the formation of the failure surface trend. As the bedding angle increases to 60° and 90°, its influence is weakened.

3.3. Analysis of Variation of Shale Mechanical Parameters with Bedding Angle. Figure 6 shows the compressive strength of shale in different directions. Dotted lines represent the sampling angle, and underlined numbers represent the average compressive strength of the group. It can be seen from the figure that the uniaxial compressive strength of outcrop shale of Longmaxi Formation is highly discrete. The uniaxial compressive strength ranges from 126 to 189 MPa, which belongs to high-strength rock.

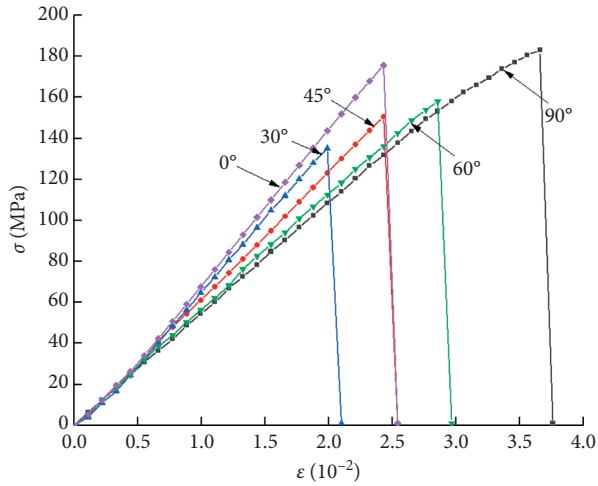

Figure 4: Stress-strain curves of shale at different bedding angles with azimuth angle $\alpha = 0^{\circ}$.

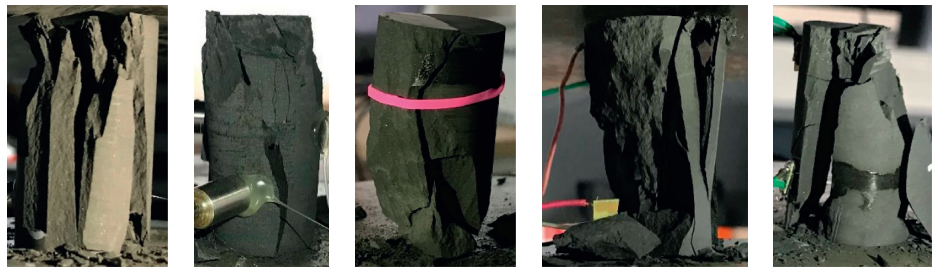

Figure 5: Failure modes of shale specimens at different bedding angles with azimuth angle $\alpha = 0^{\circ}$. (a) $\beta = 0^{\circ}$. (b) $\beta = 0^{\circ}$. (c) $\beta = 0^{\circ}$. (d) $\beta = 0^{\circ}$. (e) $\beta = 0^{\circ}$.

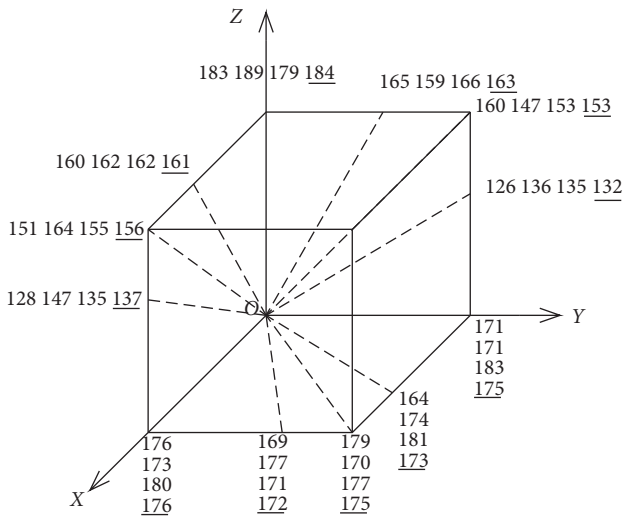

Figure 6: Compressive strength of shale in different directions.

Figure 7 shows the variation of compressive strength with bedding. The curves are plotted with the compressive strength data of bedding angle $\beta = 0^{\circ}$, 30°, 45°, 60°, and 90° at azimuth angle $\alpha = 0^{\circ}$. From the curve, it can be seen that the compressive strength of shale has a U-type change law with the increase of bedding angle. When the bedding angle is 0° and 90°, the compressive strength is higher, and the maximum value of 90° is 189 MPa. When the bedding angle is 30°, the minimum compressive strength is 126 MPa. The difference between the maximum and minimum compressive strength is 63 MPa. When the bedding angle is 45°~60°, the slope of the curve decreases, which indicates that in this interval the effect of bedding angle on compressive strength is weakened.

Figure 8 shows the variation of elastic modulus and Poisson's ratio with bedding. The curves are plotted with the elastic modulus and Poisson's ratio data of bedding angle $\beta = 0^{\circ}$, 30°, 45°, 60°, and 90° at azimuth angle $\alpha = 0^{\circ}$. The elastic modulus decreases with the increase of bedding angle, with a maximum value of 7.51 GPa at 0° and a minimum value of 5.22 GPa at 90°. The changing trend of elastic modulus is slow at both ends and fast in the middle. The change trend of Poisson's ratio is similar to that of compressive strength, showing a U-type change rule of high, middle, and low between two ends. The maximum Poisson's ratio is 0.4 at 0°, and the minimum value is 0.19 at 30°.

Table 2 records the tensile strength of outcrop shale with different bedding angles. The curve of tensile strength changing with bedding angle is drawn as shown in Figure 9. The tensile strength has strong discreteness, and the value of each group of three samples has a difference of about 1 MPa even under the same angle. In particular, the values of tensile

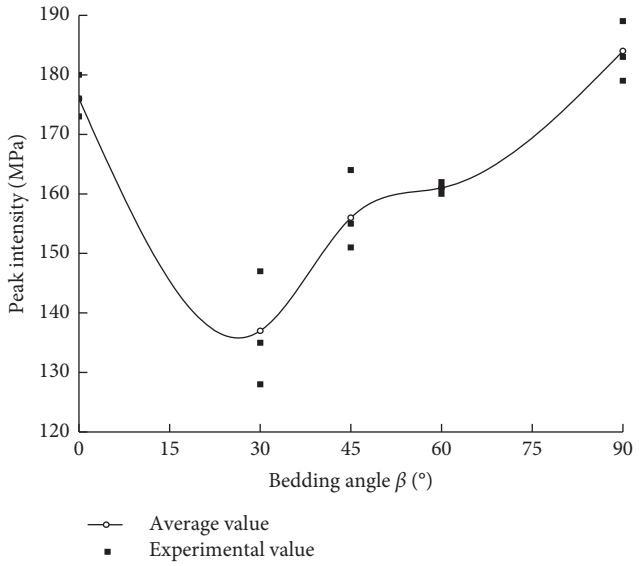

Figure 7: Compressive strength variation with bedding angle.

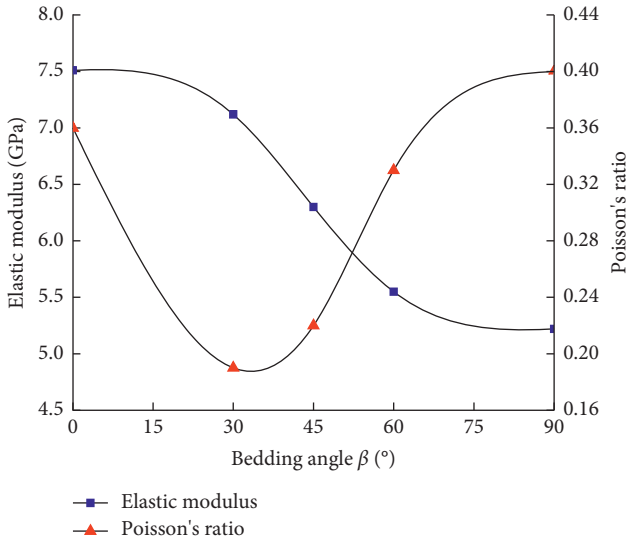

Figure 8: Elastic modulus and Poisson's ratio variation with bedding angle.

strength are more discrete at 0° and 15°. The curve shows that the tensile strength is significantly affected by bedding angle. When the bedding angle is 0°~15°, the dispersion of tensile strength value is higher but has no obvious change rule with angle. When the bedding angle increases to 30°, the tensile strength increases with the increase of bedding angle. The tensile strength value has a minimum average value of 3.82 MPa at 0°~15° and has a maximum average value of 7.59 MPa at 90°.

3.4. Analysis of Variation of Wave Velocity with Bedding Angle. Due to the energy attenuation of ultrasonic wave propagating through the weak bedding plane in shale, the velocity of ultrasonic wave propagating in shale shows anisotropic characteristics. The wave velocity of ultrasonic

Table 2: Summary of tensile strength of outcrop shale.

Bedding angle β (°)	Tensile strength (MPa)			Average value (MPa)
	1#	2#	3#	
0	3.44	4.22	3.80	3.82
15	3.33	4.35	3.98	3.88
30	4.31	5.20	4.18	4.56
45	5.68	5.81	5.88	5.79
60	6.90	6.35	6.49	6.58
75	7.62	6.98	7.26	7.28
90	7.68	7.90	7.16	7.58

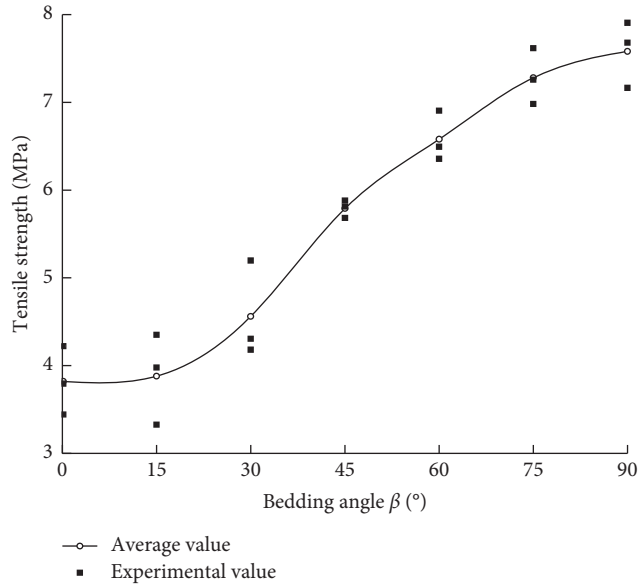

Figure 9: Tensile strength of outcrop shale variation with bedding angle.

wave passing through bedding in different directions is measured as shown in Figure 10. The test results and the variation of wave velocity with bedding angle are shown in Table 3 and Figure 11.

Figure 11 shows the variation of ultrasonic wave velocity with bedding angle. The wave velocity is obviously affected by bedding angle and decreases with the increase of bedding angle. The transverse wave velocity has a maximum value of 2586 m/s at 0° and a minimum value of 2280 m/s at 90°. There is a difference of 306 m/s between the maximum and minimum. The vertical wave velocity has a maximum value of 4820 m/s at 0° and a minimum value of 4065 m/s at 90°. There is a difference of 755 m/s between the maximum and minimum.

3.5. Difference Analysis of Mechanical Performance between Outcrop Shale and Deep Shale. In order to directly compare the differences between deep shale and outcrop shale, this paper measures the mineral composition and microstructure of deep shale and outcrop shale.

Figure 12 shows the mineral content analysis results of deep shale and outcrop shale. The deep shale is rich in brittle minerals, including quartz and feldspar, accounting for

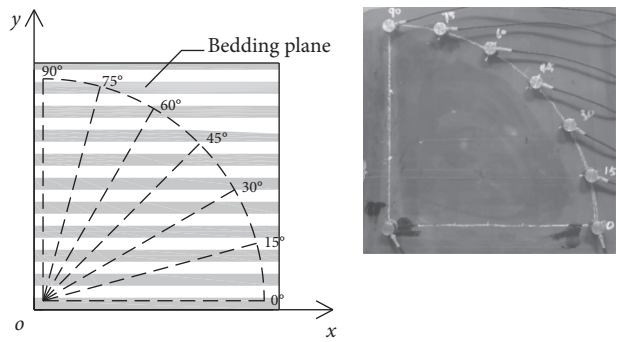

(a) (b)

Figure 10: Schematic diagram of ultrasonic wave velocity measurement.

Table 3: Shale ultrasonic wave velocity.

β (°)	Transverse wave velocity			Average value	Vertical wave velocity			Average value
0	2520	2752	2586	2619	4732	4812	4917	4820
15	2405	2552	2654	2537	4761	4703	4899	4787
30	2305	2479	2420	2401	4627	4714	4638	4659
45	2289	2458	2358	2368	4589	4500	4674	4587
60	2113	2454	2389	2318	4397	4561	4433	4463
75	2199	2342	2307	2282	4097	4161	4196	4151
90	2076	2090	2280	2148	4060	4196	3939	4065

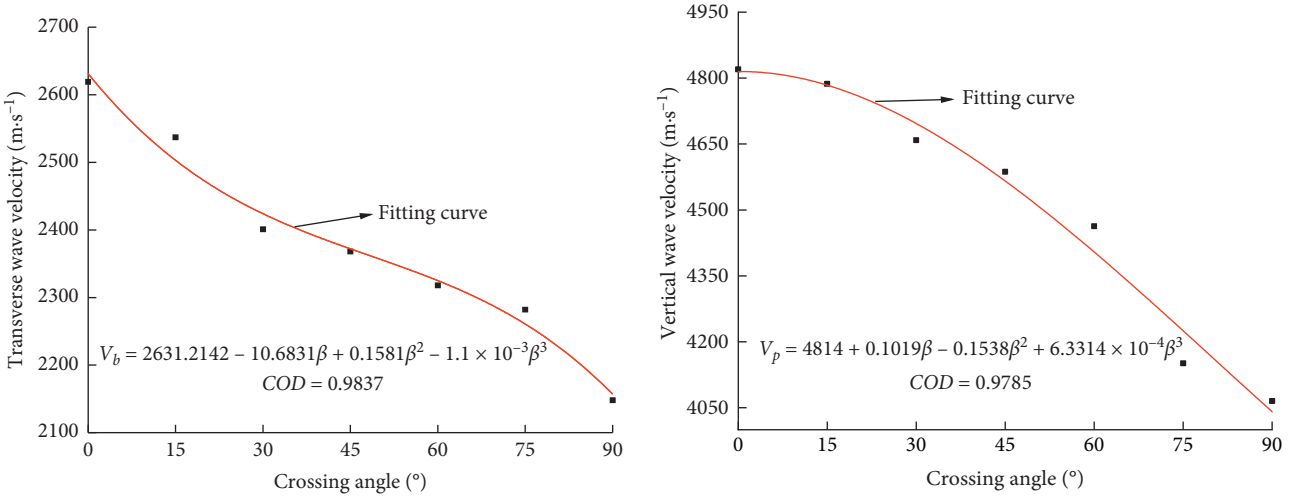

(a) (b)

Figure 11: Variation of wave velocity with bedding angle. (a) Transverse wave velocity. (b) Vertical wave velocity.

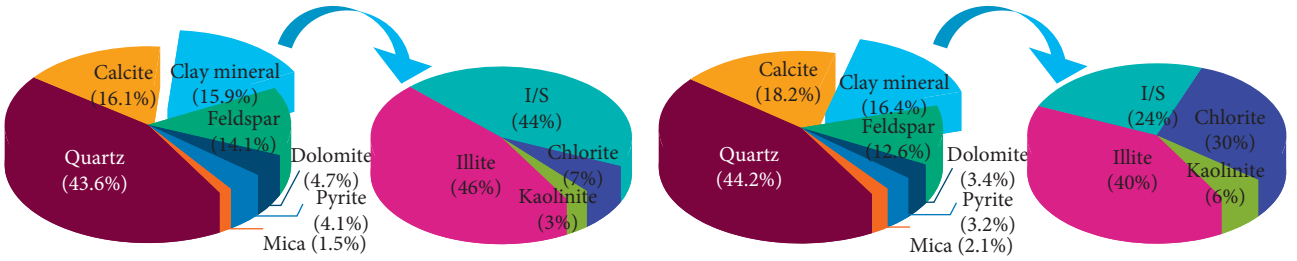

(a) (b)

Figure 12: Shale mineral content analysis results. (a) Mineral composition of deep shale in Well Yi 201. (b) Mineral composition of outcrop shale.

57.7%. Furthermore, the proportion of clay minerals is 15.9%, including illite, I/S (mixed-layer illite and smectite), chlorite, and kaolinite. The outcrop shale is rich in brittle minerals, including quartz and feldspar, accounting for 56.8%. Furthermore, the proportion of clay minerals is 16.4%, including illite, I/S, chlorite, and kaolinite. Overall, deep/outcrop shale is characterized by brittle mineral and clay mineral enrichment. Both of them have the same mineral composition and similar proportions of brittle minerals and clay minerals.

Figure 13 shows the microstructure of deep shale and outcrop shale. There is no significant difference in structure between the two at 800 magnification. No large pores or natural cracks are seen in the picture, suggesting that both shales have dense properties. At 3000 magnification, quartz and pyrite grains can be clearly observed embedded in the shale matrix. Deep shale has more lamellar foil structure than outcrop shale, and the area of asphaltene is larger than that of outcrop shale. The mineral components of outcrop shale are arranged more closely.

In this paper, the basic mechanical parameters of deep shale are measured. Since the preparation of deep samples is difficult, only samples with bedding angle 90° are obtained in this experiment, and six samples as shown in Figure 3(b). The results of uniaxial compression and Brazilian splitting tests on deep shale samples are shown in Table 4.

The data in Table 4 show that there are differences between the mechanical characteristics of deep shale and outcrop shale. Specifically, the compressive strength of deep shale is 57 MPa, which is about 1/3 of outcrop shale, and the elastic modulus is 3.56 GPa~ 4.80 GP, which is about 3/4 of outcrop shale. In addition, the tensile strength and Poisson's's ratio of deep shale and outcrop shale are close. The tensile strength ranges from 4.24 to 7.88 MPa. Poisson's ratio ranges from 0.28 to 0.36.

Figure 14 shows the stress-strain curve and postfailure morphology of deep shale in Well Lu202. When strain is less than 0.56×10^{-2}, the curvature of the curve increases gradually, which indicates that there is an obvious compaction stage in the process. When the strain is greater than 1.64×10^{-2}, the curve enters the plastic failure zone, and the curve fluctuates violently and forms two stress drops. The second drop value is relatively large, and it decreases from the peak value of 56.6 MPa to 53 MPa. At this time, the specimen does not lose the supporting force. With the increase of vertical load, when the stress gradually increases to 56 MPa, the specimen loses its supporting force instantly after failure. The whole process is characterized by plastic failure.

Figure 14(b) shows the specimen morphology after failure. The specimen has splitting failure along the direction of vertical bedding plane. The long strip broken rock block is scattered on the right side of the shale, and the left side of the failure surface is stripped of the main body to form a transverse instability failure surface in the middle part. It is considered that these two failure modes are the main reasons for the sharp fluctuation of stress-strain curve in the plastic failure zone. With the axial load gradually increases to the ultimate load-bearing capacity, the vertical splitting failure occurs in the local area around the cylindrical specimen. At this time, it is accompanied by a stress drop, but the whole specimen is not completely destroyed and still has a supporting force. With the increase of axial stress, the specimen reaches the ultimate bearing capacity and loses its supporting force. This process consists of two parts, namely, the splitting failure of the undamaged part and the instability failure of the slender shale formed by the splitting failure in the previous process.

In conclusion, there are similarities and differences in mechanical performance between deep shale and outcrop shale. The compression stage of deep shale is obvious while that of outcrop shale is not obvious. However, both of them have a long elastic stage and tend to change from elastic deformation to plastic deformation in high-stress state. Compared with outcrop shale, deep shale is accompanied by instability failure when the stress reaches the maximum bearing capacity. However, the angle between loading direction and bedding is the main factor affecting deep/outcrop shale failure mode. In terms of mechanical parameters, the compressive strength and elastic modulus of deep shale are smaller than that of outcrop shale. However, the tensile strength and Poisson's ratio in deep/outcrop shale are close to each other.

Because they have similar mineral composition, it is thought that the difference in microstructure may lead to the different mechanical performance of deep/outcrop shale. The experimental results indicate that it is feasible to study deep shale with outcrop shale as reference, but the differences of mechanical performance between outcrop shale and deep shale should be considered when applying outcrop shale research results to deep shale.

4. Anisotropic Analysis of Mechanical Parameters of Shale

The property that the mechanical parameters of shale change in one direction with the change in this direction is called anisotropy. The third section shows that the mechanical parameters of shale change with the bedding angle. The following is an analysis of the anisotropy of the mechanical parameters including compressive strength, tensile strength, elastic modulus, Poisson's ratio, brittleness, and velocity of ultrasonic wave propagation with the change of bedding angle.

4.1. Anisotropic Analysis of Compressive/Tensile Strength. Referring to the degree of strength anisotropy defined by the Saroglou and Tsiambaos [28], this paper introduces a new degree of anisotropy "A" which can measure the degree of variation of mechanical parameters with bedding angle. We define the degree of anisotropy of compressive strength as

$$A_c = \frac{\sigma_{\text{cmax}}}{\sigma_{\text{cmin}}}, \tag{1}$$

where A_c is the degree of anisotropy of compressive strength; σ_{cmax} is the maximum value of compressive strength; and σ_{cmin} is the minimum value of compressive strength.

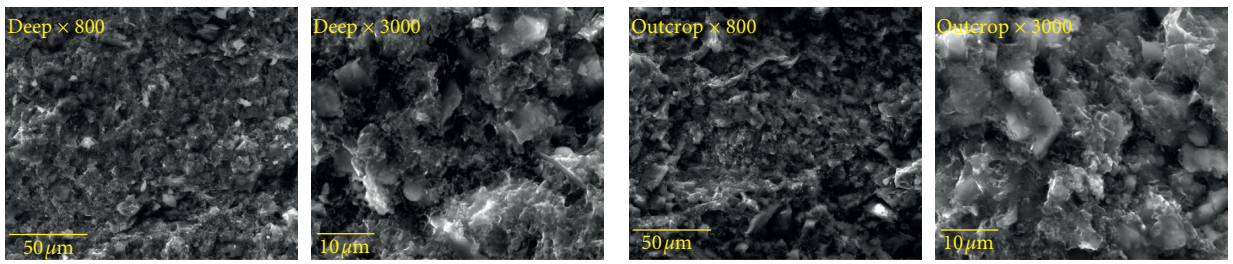

(a) (b)

Figure 13: Microstructure analysis images of shale. (a) Deep shale in Well Yi 201 SEM photos. (b) Outcrop shale SEM photos.

Table 4: Value of compressive and tensile strength of deep shale.

Location	Compressive strength (MPa)			Average value (MPa)	Elastic modulus (MPa)	Poisson's ratio
	1#	2#	3#			
Well Yi201	57	—	—	57	3560	0.28
Well Lu202	57	—	—	57	4800	0.36
	Tensile strength/MPa					
	1#	2#	3#			
Well Yi201	5.33	4.24	—	4.78	—	—
Well Lu202	7.16	7.88	—	7.52	—	—

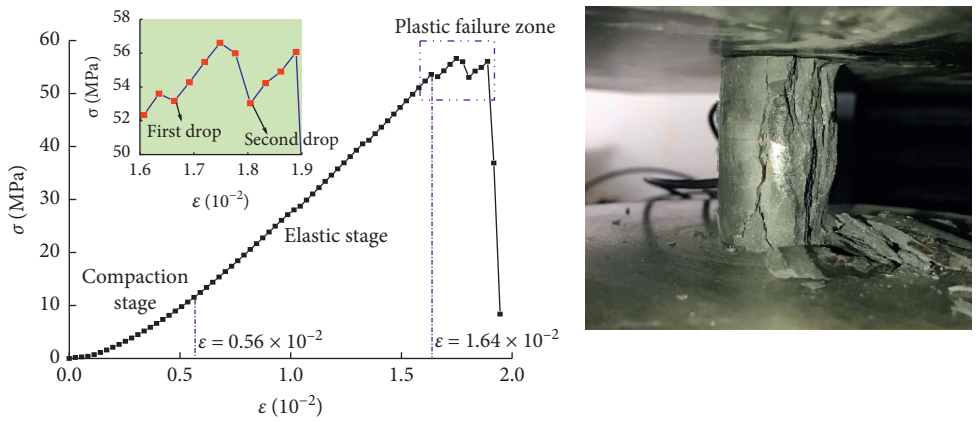

(a) (b)

Figure 14: Stress-strain curve and failure characteristics of deep shale in Well Lu 202. (a) Stress-strain curve. (b) Postdestruction form.

According to formula (1), the degree of anisotropy of compressive strength $A_C = 1.5$. Through analysis, it is considered that the angle between the bedding plane and the principal stress leads to the anisotropic characteristics of compressive strength. When the bedding angle is 30°, the shear slip failure occurs along the direction of the weak bedding plane. The compressive strength largely depends on the shear capacity of the weak bedding plane. The low shear strength of the bedding plane directly leads to the reduction of the compressive strength. When the bedding angle is 0° and 90°, the compressive strength mainly depends on the shale matrix itself, so the compressive strength is higher than that at the bedding angle of 30°.

Define the degree of anisotropy of tensile strength as

$$A_T = \frac{T_{\max}}{T_{\min}}, \tag{2}$$

where A_T is the degree of anisotropy of tensile strength; $T_{\max}$ is the maximum value of tensile strength; and $T_{\min}$ is the minimum value of tensile strength.

According to formula (2), the degree of anisotropy of shale tensile strength $A_T = 2.0$. It is considered that the

difference of failure modes under different bedding angles leads to the anisotropy of tensile strength. When the bedding angle is small, the failure mode is splitting failure along the direction of bedding plane. In this case, the tensile strength is mainly dependent on the tensile strength of weak bedding plane, so the tensile strength is lower. When the bedding angle is 90°, the failure mode of shale is splitting failure through the bedding plane. Its tensile strength is affected by the shale matrix; thus, the tensile strength increases by two times than 0°.

4.2. Analysis of Anisotropy of Elastic Modulus, Poisson's Ratio, and Brittleness Index. Similarly, the anisotropy of elastic modulus and Poisson's ratio are defined as

$$A_E = \frac{E_{\max}}{E_{\min}}, \qquad A_\upsilon = \frac{\upsilon_{\max}}{\upsilon_{\min}}, \tag{3}$$

where A_E is the degree of anisotropy of elastic modulus; $E_{\max}$ and $E_{\min}$ are the maximum and minimum values of elastic modulus; A_υ is the degree of anisotropy of Poisson's ratio; and $\upsilon_{\max}$ and $\upsilon_{\min}$ are the maximum and minimum values of Poisson's ratio.

According to formula (3), the degree of anisotropy of elastic modulus $A_E = 1.4$ and Poisson's ratio $A_\upsilon = 2.1$. The elastic modulus and Poisson's ratio reflect the brittleness of the specimen. Using the normalized average method of elastic modulus and Poisson's ratio proposed by Rickman and Mullen [29], the brittleness index of each bedding angle direction is obtained:

$$E_{no} = (E_{st} - 1)(8 - 1), \qquad \nu_{no} = (\nu_{st} - 0.4)(0.1 - 0.4), \qquad \mathrm{BI} = \frac{(E_{no} + \nu_{no})}{2}, \tag{4}$$

where BI is the brittleness coefficient; E_{st} is the static elastic modulus in 10 GPa units; υ_{st} is the static Poisson's ratio; E_{no} is the normalized elastic modulus; and υ_{no} is the normalized Poisson's ratio.

Figure 15 shows the variation of brittleness index with bedding angle. The curves are plotted with the brittleness index data of bedding angle $\beta = 0°$, 30°, 45°, 60°, and 90° at azimuth angle $\alpha = 0°$.With the change of bedding angle, the brittleness index increases first and then decreases. There is a maximum brittleness index of 0.33 in the direction of 30°, and a small brittleness index of 0.05 and 0.03 in the direction of 0° and 90°.

Define the degree of anisotropy of brittleness index as

$$A_{\mathrm{BI}} = \frac{\mathrm{BI}_{\max}}{\mathrm{BI}_{\min}}, \tag{5}$$

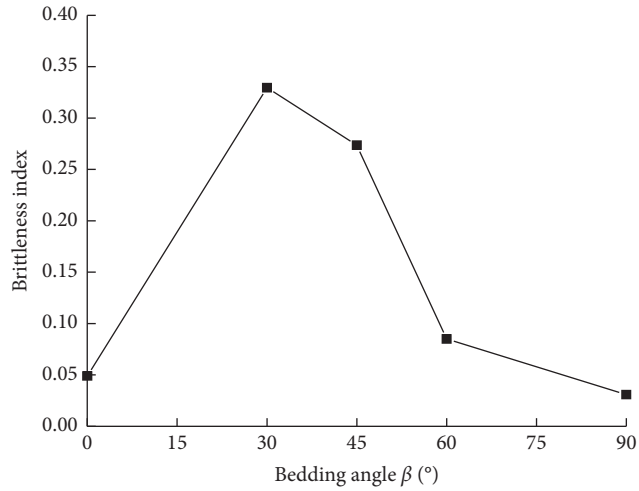

Figure 15: Variation of brittleness index with bedding angle.

where A_{BI} is the degree of anisotropy of brittleness index and $\mathrm{BI}_{\max}$ and $\mathrm{BI}_{\min}$ are the maximum and minimum values of brittleness index.

According to formula (5), the anisotropy of brittleness index $A_{\mathrm{BI}} = 11$, which indicates that bedding angle has great influence on shale brittleness index.

4.3. Analysis of Anisotropy of Ultrasonic Wave Velocity. Define the degree of anisotropy of wave velocity as

$$A_V = \frac{V_{0°}}{V_{90°}}, \tag{6}$$

where A_v is the degree of anisotropy of wave velocity; $V_{0°}$ is the velocity of ultrasonic wave in the direction of 0°; $V_{90°}$ is the velocity of ultrasonic wave in the direction of 90°.

According to formula (6), the anisotropy of transverse wave velocity $A_{\mathrm{Vb}} = 1.13$, and the anisotropy of vertical wave velocity $A_{\mathrm{Vp}} = 1.19$. After analysis, it is considered that the anisotropy of wave velocity is caused by the blocking effect of weak bedding plane. When the bedding angle is 0°, the direction of ultrasonic propagation is consistent with the direction of bedding and does not need to cross the bedding plane. When the bedding angle is 90°, the ultrasonic propagation direction is vertical to the bedding plane. In this case, the mineral components, clay, and complex spatial morphology of the bedding plane impede the propagation of waves, so the wave velocity is slower.

When the bedding angle increases from 0° to 90° the propagation direction of ultrasonic wave gradually changes from parallel bedding direction to vertical bedding direction. The number of layers of bedding plane needed to be penetrated increases, and the energy attenuation in the propagation process increases. So, the propagation velocity of wave tends to slow down gradually.

In summary, due to the differences in composition and spatial structure between the bedding plane and shale matrix, shale has different mechanical characterization along different bedding directions. In this paper, the degree of

anisotropy of mechanical parameters (compressive strength, elastic modulus, Poisson's ratio, and tensile strength), ultrasonic wave velocity, and brittleness parameters of shale are calculated. These parameters are affected by bedding plane, from high to low, which are brittleness index $A_{\mathrm{BI}} = 11$, Poisson's ratio $A_v = 2.1$, tensile strength $A_{\mathrm{T}} = 2.0$, compressive strength $A_c = 1.5$, Elastic modulus $A_E = 1.4$, vertical wave velocity $A_{\mathrm{Vp}} = 1.19$, and transverse wave velocity $A_{\mathrm{Vb}} = 1.13$.

5. Shale Constitutive Model and Parameter Calculation

Taking the bedding plane as the basic plane, the spatial coordinate system is established, as shown in Figure 2. In order to obtain the influence of the azimuth on the behavior of shale mechanics, this paper conducted two groups of experiments for comparison. The first group of experiments measured the mechanical parameters in different azimuth directions of $\alpha = 0^\circ, 30^\circ, 45^\circ, 60^\circ$, and 90° in the bedding plane (directions 1, 2, 3, 4, and 5). The second group of experiments measured the direction of the same bedding angle in two vertical planes (direction 1 and 5, 12 and 6, 11 and 7, and 10 and 8).

Figure 16 shows the variation of compressive strength with azimuth angle. The compressive strength in the direction of bedding plane is discrete, even if the three compressive strengths in the same direction are not exactly the same. Removing the deviation of compressive strength values of individual samples caused by shale discrete characteristics, the values of compressive strength fluctuate slightly with azimuth change from 163 to 183 MPa. The fluctuation range is within 12.27%, and the change trend along the azimuth direction is not obvious.

Figure 17 shows the variation of compressive strength with bedding in two vertical planes. In the direction of two identical bedding angles perpendicular to each other, the compressive strength of the shale is always similar. The compressive strength in two vertical planes has the same U-type change rule with bedding angle. The higher coincidence rate of the two U-type change rule curves indicates that the change of azimuth angle does not affect the anisotropy.

Like shale, this material has the same elastic parameters in all directions (called transverse) of the parallel bedding plane, unlike the elastic parameters in the vertical direction (called longitudinal), which is called transverse isotropic in engineering. The number of independent elastic constants for transverse isotropies decreases from 21 to 5 compared to extreme anisotropic elastomers [30].

As shown in Figure 18, a transverse isotropic coordinate system consists of a global coordinate system (x, y, z) and a local coordinate system (x', y', z'). In the local coordinate system (x', y', z'), the z' axis and the normal direction of the bedding plane are the same, while the x' axis and y' axis are located in the bedding plane, and the stress-strain relationship can be expressed by the following formula [31]:

$$\{\varepsilon'\} = D'^{-1}\{\sigma'\}, \tag{7}$$

where ε' is the strain tensor; D'^{-1} is the flexibility matrix; and σ' is the stress tensor:

$$D'^{-1} = \begin{bmatrix} \frac{1}{E_1} & -\frac{v_1}{E_1} & -\frac{v_2}{E_2} & 0 & 0 & 0 \\ -\frac{v_1}{E_1} & \frac{1}{E_1} & -\frac{v_2}{E_2} & 0 & 0 & 0 \\ -\frac{v_2}{E_2} & -\frac{v_2}{E_2} & \frac{1}{E_2} & 0 & 0 & 0 \\ 0 & 0 & 0 & \frac{1}{G_1} & 0 & 0 \\ 0 & 0 & 0 & 0 & \frac{1}{G_2} & 0 \\ 0 & 0 & 0 & 0 & 0 & \frac{1}{G_2} \end{bmatrix}, \tag{8}$$

where E_1 is the elastic modulus in the bedding plane; E_2 is the elastic modulus perpendicular to bedding direction; v_1 is Poisson's ratio in the bedding plane; v_2 is Poisson's ratio perpendicular to bedding direction; G_1 is the shear modulus in the bedding plane; and G_2 is the shear modulus perpendicular to bedding direction.

Because $G_1 = E_1/2(1+v_1)$, G_1 is not an independent elastic constant. To describe the transversely isotropic elastic body of shale, there are only 5 independent elastic constants E_1, E_2, v_1, v_2, and G_2. The first four parameters can be directly measured by the bedding angle $\beta = 0^\circ$ and 90° samples. The shear modulus perpendicular to the bedding direction G_2 can be obtained by fitting the elastic modulus in the direction of multiple bedding angles.

By means of coordinate system transformation, Niandou et al. [13] obtained the elastic modulus E_β of transversely isotropic body under any bedding angle:

$$\frac{1}{E_\beta} = \frac{1}{E_1}\sin^4\beta + \left(\frac{1}{G_2} - \frac{2v_2}{E_2}\right) sin^2\beta\,\cos^2\beta + \frac{1}{E_2}\cos^4\beta. \tag{9}$$

The following formula can be obtained from formula (9):

$$\frac{1}{E_\beta} = \left(\frac{1}{E_1} - \frac{1}{G_2} + \frac{2v_2+1}{E_2}\right) sin^4\beta + \left[\frac{1}{G_2} - \frac{2(v_2+1)}{E_2}\right]\sin^2\beta + \frac{1}{E_2}. \tag{10}$$

Formula (10), it can be rewritten into the following form:

$$\frac{1}{E_\beta} = f\left(\sin^2\beta\right). \tag{11}$$

As shown in Figure 19, the reciprocal elastic modulus of Longmaxi Formation outcrop shale under different bedding angles is fitted by the least square method. The following

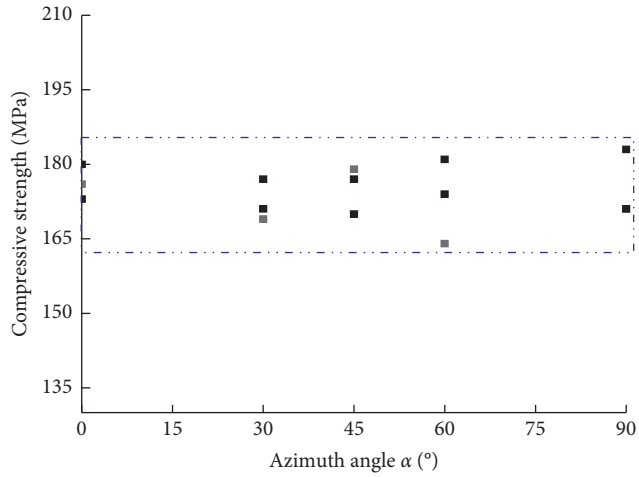

Figure 16: Variation of compressive strength with azimuth angle.

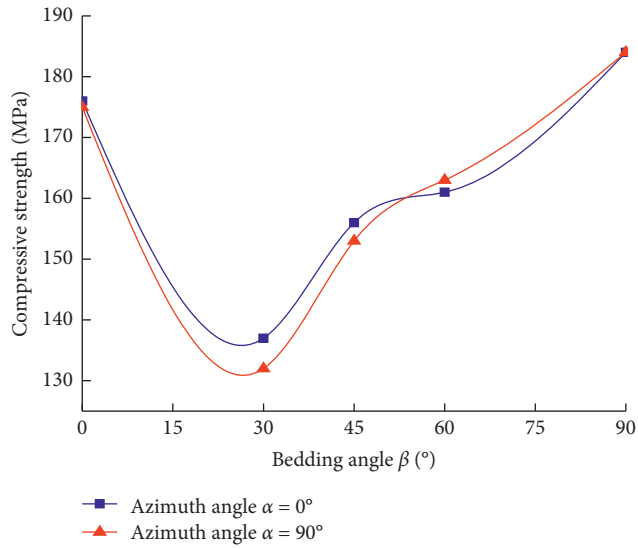

Figure 17: Variation of compressive strength with bedding in two vertical planes.

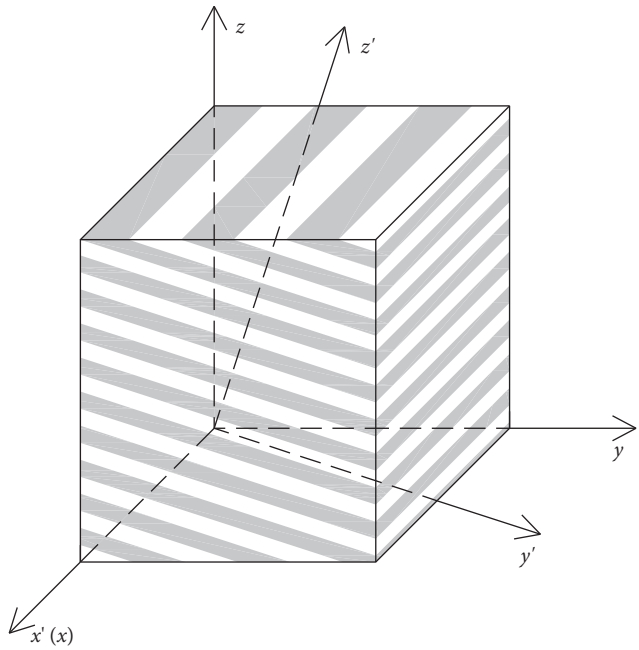

Figure 18: Transversely isotropic material coordinate system.

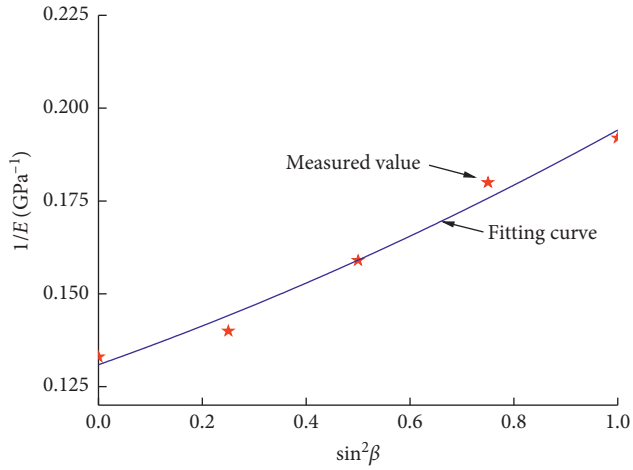

Figure 19: Reciprocal fitting curve of elastic modulus.

Table 5: Five elastic constants of outcrop shale of Longmaxi Formation.

E_1 (GPa)	E_2 (GPa)	υ_2	υ_2	G_2 (GPa)
7.51	5.22	0.36	0.40	1.93

formula (12) of reciprocal elastic modulus can be obtained, and the COD is 0.9827:

$$\frac{1}{E_\beta} = 0.1309 + 0.0495 \sin^2 \beta + 0.0137 \sin^4 \beta, \quad (12)$$

where E_β is the elastic modulus in the direction of β angle with bedding plane.

By comparing the fitting curve formula (12) with formula (11), the elastic constant G_2 can be retrieved. 5 independent elastic constants of outcrop shale of Longmaxi Formation can be obtained as shown in Table 5.

6. Conclusion

(1) The stress-strain curve of outcrop shale has no obvious compaction stage. The elastic stage is longer, and the distinction between elastic stage and plastic stage is not obvious. With the increase of bedding angle, the deformation mode trends to from elastic deformation to plastic deformation in high-stress state. The larger the bedding angle, the longer the plastic deformation stage.

(2) When the bedding angle is 0°, 30°, and 45°, the direction of failure plane is basically the same as that of bedding plane. Tensile failure and shear failure occur along the bedding direction, and the bedding plane plays a leading role in the formation of failure surface. When the bedding angle is 60° and 90°, the influence of the bedding plane on the trend of failure surface is weakened. Under the action of the maximum principal stress, the inclined shear failure surface along the bedding plane and the vertical tensile splitting failure surface along the direction of maximum principal stress are produced.

(3) The anisotropy of mechanical parameters of shale along different directions of bedding angle is obvious. Tensile strength, elastic modulus, and ultrasonic wave velocity decrease with the increase of bedding angle. Compressive strength and Poisson's ratio show a U-type change pattern, which are higher at 0°/90° and lower at 30°. The angle of anisotropy of mechanical parameters affected by bedding from high to low is brittleness index, Poisson's ratio, tensile strength, compressive strength, elastic modulus, vertical wave velocity, and transverse wave velocity.

(4) The similarities between the deep shale and the outcrops are that the tensile strength and Poisson's ratio. Their stress-strain curves have a long elastic stage and change from elastic deformation to plastic deformation under high-stress state. The difference between deep shale and outcrop shale shows that the stress-strain curve of deep shale has obvious compaction stage. The compressive strength and elastic modulus of deep shale are only 1/3 and 3/4 of outcrop shale. In failure mode, the deep shale is accompanied by destabilization failure when the stress reaches the maximum bearing capacity. The reason for this phenomenon may be the difference in microstructure between deep shale and outcrop shale.

(5) Shale belongs to the transverse isotropy in engineering material. The change of azimuth angle will not affect the mechanical parameters of shale in this direction. Outcrop shale of Longmaxi Formation has five elastic constants based on transverse isotropic model: $E_1 = 7.51$ GPa, $E_2 = 5.22$ GPa, $\upsilon_1 = 0.36$, $\upsilon_2 = 0.40$, and $G_2 = 1.93$ GPa.

Data Availability

The data used to support the findings of this study are available from the corresponding author upon request.

Conflicts of Interest

The authors declare that they have no conflicts of interest.

Acknowledgments

The authors gratefully acknowledge the financial support given by the China National Science and Technology Major Project (grant no. 2017ZX05037001) and the Project of Discipline Innovation Team of Liaoning Technical University (grant no. LNTU20TD-11).

References

[1] Y. Chen, J. T. Xu, and P. Wang, "Shale gas potential in China: a production forecast of the Wufeng-Longmaxi Formation and implications for future development," *Energy Policy*, vol. 147, p. 11, Article ID 111868, 2020.

[2] H. Liu, S. W. Meng, J. Su, G. M. Zhang, and L. Chen, "Reflections and suggestions on the development and engineering

management of shale gas fracturing technology in China," *Natural Gas Industry*, vol. 39, no. 4, pp. 1–7, 2019.

[3] J. F. W. Gale, R. M. Reed, and J. Holder, "Natural fractures in the Barnett Shale and their importance for hydraulic fracture treatments," *AAPG Bulletin*, vol. 91, no. 4, pp. 603–622, 2019.

[4] M. Josh, L. Esteban, C. Delle Piane, J. Sarout, D. N. Dewhurst, and M. B. Clennell, "Laboratory characterisation of shale properties," *Journal of Petroleum Science and Engineering*, vol. 88-89, pp. 107–124, 2019.

[5] T. J. Katsube, B. S. Mudford, and M. E. Best, "Petrophysical characteristics of shales from the Scotian shelf," *Geophysics*, vol. 56, no. 10, pp. 1681–1689, 1991.

[6] X. Liu, W. Zeng, L. Liang, and M. Lei, "Wellbore stability analysis for horizontal wells in shale formations," *Journal of Natural Gas Science and Engineering*, vol. 31, pp. 1–8, 2016.

[7] J. C. Jaeger, N. G. W. Cook, and R. W. Zimmerman, *Fundamentals of Rock Mechanics*, Blackwell Publishing, Malden, MA, USA, 4th edition, 2007.

[8] S. G. Lekhnitskii, P. Fern, J. J. Brandstatter, and E. H. Dill, "Theory of elasticity of an anisotropic elastic body," *Physics Today*, vol. 17, no. 1, p. 84, 1964.

[9] R. Nova, "The failure of transversely isotropic rocks in triaxial compression," *International Journal of Rock Mechanics and Mining Sciences & Geomechanics Abstracts*, vol. 17, no. 6, pp. 325–332, 1980.

[10] O. Cazacu, N. D. Cristescu, and J. F. Shao, "A new failure criterion for transversely isotropic rocks," *International Journal of Rock Mechanics & Mining Sciences*, vol. 35, no. 4, p. 421, 1996.

[11] Y.-K. Lee and S. Pietruszczak, "Tensile failure criterion for transversely isotropic rocks," *International Journal of Rock Mechanics and Mining Sciences*, vol. 79, pp. 205–215, 2015.

[12] L. Vernik and A. Nur, "Ultrasonic velocity and anisotropy of hydrocarbon source rocks," *Geophysics*, vol. 57, no. 5, pp. 727–735, 1992.

[13] H. Niandou, J. F. Shao, J. P. Henry, and D. Fourmaintraux, "Laboratory investigation of the mechanical behaviour of Tournemire shale," *International Journal of Rock Mechanics and Mining Sciences*, vol. 34, no. 1, pp. 3–16, 1997.

[14] J. W. Cho, H. Kim, S. Jeon, and K. Min, "Deformation and strength anisotropy of Asan gneiss, Boryeong shale, and Yeoncheon schist," *International Journal of Rock Mechanics and Mining Sciences (1997)*, vol. 50, pp. 158–169, 2012.

[15] H. Sone and D. Z. Mark, "Mechanical properties of shale-gas reservoir rocks-Part 1: static and dynamic elastic properties and anisotropy," *Geophysics*, vol. 78, no. 5, pp. 381–392, 2013.

[16] G. R. Chalmers, R. M. Bustin, and I. M. Power, "Characterization of gas shale pore systems by porosimetry, pycnometry, surface area, and field emission scanning electron microscopy/transmission electron microscopy image analyses: examples from the Barnett, Woodford, Haynesville, Marcellus, and Doig units," *AAPG Bulletin*, vol. 96, no. 6, pp. 1099–1119, 2012.

[17] C. B. Li, H. P. Xie, and J. Wang, "Anisotropic characteristics of crack initiation and crack damage thresholds for shale," *International Journal of Rock Mechanics and Mining Sciences*, vol. 126, p. 9, Article ID 104178, 2020.

[18] P. Wang, F. Ren, S. Miao, M. Cai, and T. Yang, "Evaluation of the anisotropy and directionality of a jointed rock mass under numerical direct shear tests," *Engineering Geology*, vol. 225, pp. 29–41, 2017.

[19] Z. Jin, W. Li, C. Jin, J. Hambleton, and G. Cusatis, "Anisotropic elastic, strength, and fracture properties of Marcellus shale," *International Journal of Rock Mechanics and Mining Sciences*, vol. 109, pp. 124–137, 2018.

[20] J. Tang and G. C. Wu, "Stress-dependent anisotropy of mudstone and shale with low porosity," *Chinese Journal of Geophysics*, vol. 58, no. 8, pp. 2986–2995, 2015.

[21] T. Ma, N. Peng, Z. Zhu, Q. Zhang, C. Yang, and J. Zhao, "Brazilian tensile strength of anisotropic rocks: review and new insights," *Energies*, vol. 11, no. 2, p. 304, 2018.

[22] J. Gui, T. Ma, P. Chen, H. Yuan, and Z. Guo, "Anisotropic damage to hard brittle shale with stress and hydration coupling," *Energies*, vol. 11, no. 4, p. 926, 2018.

[23] T. Ma, C. Yang, P. Chen, X. Wang, and Y. Guo, "On the damage constitutive model for hydrated shale using CT scanning technology," *Journal of Natural Gas Science and Engineering*, vol. 28, pp. 204–214, 2016.

[24] Y. Wan, Z. Pan, S. Tang, L. D. Connell, D. D. Down, and M. Camilleri, "An experimental investigation of diffusivity and porosity anisotropy of a Chinese gas shale," *Journal of Natural Gas Science and Engineering*, vol. 23, pp. 70–79, 2015.

[25] X. Ma, "Enrichment laws and scale effective development of shale gas in the southern Sichuan Basin," *Natural Gas Industry B*, vol. 6, no. 3, pp. 240–249, 2019.

[26] H. Y. Wang, Z. S. Shi, Q. Zhao et al., "Stratigraphic framework of the Wufeng-Longmaxi shale in and around the Sichuan Basin, China: implications for targeting shale gas," *Energy Geoscience*, vol. 1, no. 3-4, pp. 124–133, 2020.

[27] GB/T. 50266-2013, *Standard for Test Methods of Engineering Rock Mass*, ASTM International, West Conshohocken, PA, USA, 2013.

[28] H. Saroglou and G. Tsiambaos, "A modified Hoek-Brown failure criterion for anisotropic intact rock," *International Journal of Rock Mechanics and Mining Sciences*, vol. 45, no. 2, pp. 223–234, 2008.

[29] R. Rickman, M. J Mullen, J. E. Petre et al., "A practical use of shale petrophysics for stimulation design optimization: all shale plays are not clones of the Barnett Shale," in *Proceedings of the SPE Annual Technical Conference and Exhibition*, September 2008.

[30] W. Q. Chen, J. Zhu, and X. Y. Li, "General solutions for elasticity of transversely isotropic materials with thermal and other effects: a review," *Journal of Thermal Stresses*, vol. 42, no. 1, pp. 90–106, 2019.

[31] H. J. Ding, W. Q. Chen, and L. Zhang, *Elasticity of Transversely Isotropic Materials*, Vol. 126, Springer Science & Business Media, Berlin, Germany, 2006.